2018

Imaging cortical dynamics in GCaMP transgenic rats with a head-mounted widefi...

HHS Public Access

Author manuscript

Neuron. Author manuscript; available in PMC 2019 December 05.

Published in final edited form as:

Neuron. 2018 December 05; 100(5): 1045–1058.e5. doi:10.1016/j.neuron.2018.09.050.

Imaging cortical dynamics in GCaMP transgenic rats with a head-mounted widefield macroscope

Benjamin B. Scott[1,2,3,6], **Stephan Y. Thiberge**[1,2,6], **Caiying Guo**[4,5], **Dougal G.R. Tervo**[4,5], **Carlos D. Brody**[1,2,3,5], **Alla Y. Karpova**[4,5], and **David W. Tank**[1,2,3,7,*]

[1]Princeton Neuroscience Institute

[2]Bezos Center for Neural Circuit Dynamics

[3]Department of Molecular Biology University, Princeton, New Jersey 08544, USA

[4]Janelia Research Campus, 19700 Helix Dr., Ashburn, VA 20147, USA

[5]Howard Hughes Medical Institute

[6]These authors contributed equally

[7]Lead Contact

Summary:

Widefield imaging of calcium dynamics is an emerging method for mapping regional neural activity but is currently limited to restrained animals. Here we describe cScope, a head- mounted widefield macroscope developed to image large-scale cortical dynamics in rats during natural behavior. cScope provides a 7.8 by 4 mm field of view, dual illumination paths for both fluorescence and hemodynamic correction, and can be fabricated at low cost using readily attainable components. We also report the development of Thy-1 transgenic rat strains with widespread neuronal expression of the calcium indicator GCaMP6f. We combined these two technologies to image large-scale calcium dynamics in the dorsal neocortex during a visual evidence accumulation task. Quantitative analysis of task-related dynamics revealed multiple regions having neural signals that encode behavioral choice and sensory evidence. Our results provide a new transgenic resource for calcium imaging in rats and extend the domain of head-mounted microscopes to larger-scale cortical dynamics.

[*]Correspondence: dwtank@princeton.edu (D.W.T.).

Author contributions

DWT and SYT conceived and designed cScope optical instrumentation. CG, DGRT, and AYK developed the Thy1-GCaMP transgenic strains, which were characterized by BBS and DGRT. SYT, BBS and DWT tested the recording system and implemented iterative design modifications. BBS and SYT performed the rat cortex imaging experiments and analyzed the data. CDB provided the high throughput facility for training and behavioral testing. BBS, SYT, and DWT wrote the paper.

Declaration of Interests

The authors declare no competing interests.

Introduction

Widefield optical imaging has emerged as a powerful method for the measurement of neural activity at the mesoscopic scale (hundreds of microns to centimeters) (Grinvald et al., 1986). Functional imaging on the mesoscopic scale has provided a wealth of information about the organization of the nervous system, from discovery of pinwheel centers in the visual cortex (Bonhoeffer and Grinvald 1991) to the characterization of cortical, retinal and spinal cord waves during development (Yuste et al., 1995; Wong et al., 1995; Feller et al., 1996; Gu et al., 1994). Functional maps and global dynamics can be obtained by recording a variety of signals from calcium dependent fluorescence changes in synthetic and genetically encoded probes to changes in the absorption and scattering of light due to changes in blood flow and the oxygenation level of hemoglobin (Ma et al., 2016).

Mesoscale imaging has been increasingly applied to measurement of brain dynamics during behavior in rodents (Wekselblatt et al., 2016). In these experiments, forced restraint is commonly used to stabilize the position of the head and brain relative to the imaging system. Virtual reality and voluntary head restraint have been used to expand the range of behaviors that can be studied using conventional widefield imaging systems (Murphy et al., 2016; Pinto et al., Society for Neuroscience Abstract 2017). Head-mounted microscopes provide an alternative to head restraint allowing neural dynamics to be imaged in an expanded range of behaviors and behavioral states, such as real-world navigation, social interactions and sleep. A variety of miniaturized implantable fluorescence microscopes have been developed to record calcium signals (Ghosh et al. ,2011; Ziv and Ghosh 2015; Cai et al., 2016; Liberti et al., 2017; Skocek et al., 2018); however, these microscopes are designed for cellular resolution imaging and thus have a relatively small field of view (FOV <1mm^2 diameter), they further lack the functionality to correct for contamination caused by the hemodynamic response, limiting their usefulness in recording large scale dynamics. Several other head mounted technologies have been developed to record widefield dynamics (Miao et al., 2017; Ferezou et al., 2006), however, none combine the ability to record fluorescence imaging and hemodynamics correction in freely moving animals.

Here we report two novel technologies that facilitate largescale imaging in rats during behavior (Figure 1). The first is, cScope, a head mounted macroscope allowing widefield imaging of the cortex (>30 mm^2) without the need for head restraint. The device consists of a 3D printed plastic macroscope body holding the optics, two independent illumination sources for intrinsic signal imaging using reflectance and fluorescence imaging using genetically encoded calcium sensors, and an imaging sensor and its readout electronics. The second technology is strains of transgenic rats that express the genetically encoded calcium sensor GCaMP6f (Chen et al., 2013) under the Thy-1 enhancer (Feng et al., 2000). These rats exhibit expression of GCaMP6f across the neocortex, hippocampus, cerebellum and other regions that was strong enough to enable two-photon cellular resolution imaging (2PM) and single-photon widefield mapping of the cortex. Together, the development of a head mounted widefield macroscope and transgenic rats expressing genetically encoded calcium indicators allow stable, high signal to noise imaging across multiple cortical regions during behavior, which we demonstrate by mapping region specific differences in activation during an accumulation of evidence task. These technologies expand the domain of head

mounted microscopes to imaging mesoscale brain dynamics and improve the toolkit for cellular resolution imaging in rats.

Results

Design of cScope, a compact head-mounted widefield macroscope

Our goal was to produce a macroscope with a FOV large enough to image multiple sensory, motor and association regions simultaneously while minimizing its overall weight as well as the torque it creates on the animal's head. We call this cortical macroscope, cScope, to reflect its utility in imaging a large portion of the neocortical surface during behavior. A maximum weight of 35g was set based on existing head mounted electrode devices (Kloosterman et al., 2009; Aronov and Tank 2014). A value of 25mm above the cranial window was considered for the center of mass maximal height. The targeted resolution was set to 20 μm, a relatively high value considering the nature of the application. Aiming for the highest fluorescence collection efficiency possible, we set a lower acceptable limit to the numerical aperture (NA) at 0.1. cScope should also be absolutely light tight. This not only would prevent environmental light from reaching the imaging sensor and corrupting the measurements, but, if done properly, would also allow experiments involving visual stimuli to be performed. Additional considerations were given to the handling of cScope. A single experimenter should be able to install it and remove it from the animal's head. These two operations should be executable in a brief period of time in order to minimize animal stress. A final consideration in the design of cScope was to ease its dissemination which involves minimizing its cost. For this reason, we chose not to use custom optics but to rely only on commercially available lenses.

The optical assembly was designed using OpticStudio 16 (Zemax). The resulting imaging path is shown in Figure 2A. Part of the optical design is a 3 mm thick glass window permanently implanted over the brain area to be imaged following the procedure described in the method section. The thickness of the glass was selected to provide a high NA and a large FOV. This window is in apposition to the first optical element on the removable macroscope assembly when it is mounted on the subject. The imaging path has a total of seven lenses, all commercially available. Reaching 67mm in length, it is folded with a dichroic mirror in its middle to lower the center of mass (Figure 2A).

Capitalizing on an existing open source head mounted imaging system, cScope uses the printed circuit board (PCB) mounted camera chip, data acquisition device hardware and software developed by the "miniscope" project (miniscope.org). The specific CMOS sensor contains 758 by 480 pixels of size 6 μm. Its rectangular shape is limiting the visible FOV of our macroscope. Stitching together images taken at different angular positions of the camera sensor (Figure S1A), the optical systems full FOV (7.8mm diameter) can be revealed. The dimensions of the visualized brain area are large in comparison to typical sensor size so, in effect, we have designed a de-magnifying instrument (0.70X on the optical axis). The image of a grid as shown Figure S1D reveals the presence of barrel deformation indicative of a decrease of magnification with distance from the optical axis. While at the center, the sensor 6 μm large pixels represent 8.6 μm large areas in the brain, pixels at the edge of the field of view represent 9.3 μm specimen regions, a reduction of the magnification to 0.64X. The

barrel deformation can be easily characterized and corrected post acquisition (Figure S1D, see methods).

Aside from image deformation, cScope was designed to minimize all other non-chromatic aberrations: spherical, astigmatism, coma and field curvature (Figure S1C). The resulting solution achieves resolution properties above the necessary requirements for our application (Figure S1B). The graph in Figure S1B relates the percentage of specimen contrast transferred to the image as a function of the period of line grating. It is known as the Contrast Transfer Function and was measured using a Siemens star target. The value this function reaches zero indicates the resolution of the system. Here, we found this value to be around 70 lines pair per mm, or 14 μm. Direct observation of 1951 resolution USAF test target confirms this measurement.

The Zemax model predicts that the NA has a minimum of 0.15 at the edge of the field of view, and a maximum of 0.22 at the center, resulting in a fluorescent signal collection twice higher at this location (Figure S1E). Imaging of a thin fluorescein solution sample illuminated by an external homogeneous light source confirms experimentally the magnitude of this variation across the field of view.

The fluorescence light source is a PCB mounted LED which was also adapted from the "miniscope.org" project. Two additional lenses to properly direct the LED light, and an excitation filter to narrow its spectral band are positioned above the dichroic filter (Figure 2B and Figure S2C). As with any imaging system, the ability to gather signal is not constant across the full field of view. We quantified these variations detailing the individual contributions of the fluorescence excitation light intensity profile and the spatial profile of collection efficiency in Figure S1E.

We found that a single filter was not sufficient at filtering out the background signal and added in our design a second one in close proximity to the imaging sensor (Figure 2B and Figure S2B).

The structural parts (Figure 2B-2C) were designed using Autodesk Inventor. In order to produce a lightweight, compact and light-shielded assembly, the mechanical parts of cScope require a complex design that can be produced at a reasonable cost by 3D printing. We determined that stereolithography, a process that uses liquid photopolymer cured by a UV laser beam and post cured at elevated temperature, gave sufficient precision and reproducibility for the macroscope body.

The fully assembled device, is comprised of three components: 1) the macroscope body, described above, 2) the headplate and glass window surgically implanted on to the skull of the animal and 3) a hemodynamic illumination collar (Figure 2C and S2A). The illumination collar screws onto the head plate and serves two functions (Figure 2B and 2C). First it acts as a mechanical support for the macroscope body. Second it houses a ring of four 530 nm LEDs used for reflectance illumination of cortical intrinsic signal changes used for hemodynamic correction. Before each imaging session the experimenter attaches the macroscope body to the collar locking it in place with a set screw. A set of pins attached to the macroscope body connect to their counterpart located in the illumination collar

providing current to power the 530 nm LED circuit. At the end of the imaging session the experimenter replaces the macroscope body with a dust cover that provides protection to the cranial window and LEDs while the rat is returned to its home cage (Figure S3).

Green 530 nm LEDs, for intrinsic imaging, and the blue 480 nm LED, for fluorescence imaging, are powered by independent MOSFET operated circuits controlled by an Arduino board receiving the firing output signal of the CMOS camera (Figure S2H). This circuitry also correctly times the LED power relative to the integration frame time of the camera and produces alternation of illumination at the two wavelengths.

The weight of the macroscope including the head plate, the window, the collar, and the small portion of cable carried by the animal sums up to 33 g. This weight is lower than several head mounted motorized microdrive electrode arrays (Yamamoto and Wilson 2008, Aronov and Tank 2014), and, in proportion to the animal weight, comparable to mouse head mounted microscopes (Cai et al., 2016). We therefore expected the apparatus to have negligible effect on the animal behavior.

The complete part list, CAD models, 3D printing ready formatted files, as well as a detailed procedure to assemble all the components are available online (see methods). An overview of the assembly steps is shown in Figure S2.

We developed both an 8 by 8 mm and an 8 by 4mm cranial window procedure for cortical imaging. Custom cranial windows were implanted over dorsal cortex, allowing optical access to up to 10% of the total cortical surface area (Figure S1A). These windows could be implanted over the midline using a modified procedure for bone removal over the sagittal sinus to prevent bleeding (Low et al., 2014), allowing simultaneous imaging of both left and right cerebral hemispheres. These implants were stable, allowing optical access to the cortical surface for more than 3 months after surgery.

Development of transgenic rats expressing GCaMP6f in neurons

In rats, expression of genetically encoded calcium sensors (GECIs) is typically achieved using direct injection of AAVs carrying the GECI transgene (Scott et al., 2013). However, since the imaging field of view possible with cScope greatly exceeds the region of tissue labeled by standard AAV-based expression techniques (typically <1mm diameter), we sought an alternative labeling strategy. One approach to achieve broader tissue expression is the production of transgenic animals, in which pan-neuronal enhancers drive GECI expression throughout the nervous system. This technique has been widely used in mice (Madisen et al., 2015), zebrafish (Ahrens et al., 2012), *C. elegans* and *d. Melanogaster* (Tian et al., 2009), however, as yet, no transgenic rats expressing GECIs have been produced.

We generated strains of rats that carry the gene for GCaMP6f under control of the Thy-1 enhancer. Linearized DNA containing the expression cassette was injected into single cell embryos and returned to host mothers. After birth, rats derived from injected embryos were screened by PCR for presence of the integrated transgene. Upon sexual maturation, founders were bred to wild type rats and progeny (F1) were examined for transgene expression by fluorescence microscopy. Two strains, Thy1-GCaMP6f-7 (Figure 3) and Thy1-GCaMP6f-9

(Figure 4), were identified that exhibited strong GCaMP6f expression in the cerebral cortex and other forebrain regions.

Analysis of histological sections revealed that both strains exhibited strong transgene expression in deep and superficial neocortical layers (Figure 3B-3D,4B), hippocampus (Figure 3E-G,4C) and the cerebellum (Figure 4D). Labeled cells also expressed the neuronal marker NeuN. In the cortex, the position and morphology of labeled cells was consistent with a pyramidal neuron phenotype in layer 2/3 and layer 5. In the hippocampus, GCaMP expression was prominent in the pyramidal layer of CA1 and in the granule cells of the dentate gyrus. As expected from similar techniques used in mice (Feng et al., 2000; Dana et al., 2014), each rat strain differed in the level and spatial distribution of GCaMP6f. For example, in the Thy1–1- GCAMP6f-9 line, expression was particularly strong in cerebellar granular cells (Figure 4D right panel). This analysis suggested these transgenic rats exhibited strong neuronal expression of GCaMP6f throughout the forebrain and motivated us to examine fluorescence signals in vivo.

To determine whether transgene expression was strong enough to enable widefield imaging of mesoscale calcium dynamics we used a single photon approach to map the boundaries of the primary visual cortex (Figure 5A-5D). Anesthetized rats (n=5) viewed an LCD screen as a checkerboard stimulus drifted across the visual field in each the four cardinal directions (Figure 5A). While rats viewed the stimulus we imaged GCaMP fluorescence changes in a 4 by 4 mm region centered on the boundary between the primary visual cortex (V1) and the medial portion of the secondary visual cortex (mV2) using a table top widefield microscope (see methods). The stimulus produced large amplitude fluorescence dynamics allowing retinotopic mapping of V1 and portions of V2 (Figure 5B-5D). The size, orientation and position of V1 was similar across all rats and consistent with previously described retinotopic maps produced by single unit electrophysiological recordings (Espinoza and Thomas 1983) and intrinsic imaging (Gias et al., 2005).

Although our focus in the present study is on widefield imaging, we also evaluated Thy1-GCaMP6f-7 rats for cellular resolution functional imaging in cortical neurons using 2PM in Thy1- GCaMP6f-7 rats (see methods). GCaMP labeled neurons were readily observed in superficial layer 2/3 using conventional 2PM techniques and all neurons examined exhibited nuclear exclusion of GCaMP fluorescence (Figure 5E). Transgene expression was widespread and relatively homogeneous across dorsal cortex (Figure 5F). Labeling was sufficient to allow recording of spontaneous dynamics and evoked responses from neurons 200 μm deep with conventional 2PM (Figure S4A-S4B and Movie S1). GCaMP expression did not produce obvious signs of toxicity, including nuclear localization of GCaMP fluorescence or epileptiform activity (Figure S4C-S4D). Variability in expression levels between animals (Table 2) was similar to that seen using the Thy-1 enhancer to drive GCaMP6f expression in transgenic mice (Dana et al., 2014). Together, these results suggested that these transgenics present a potentially useful alternative to viral labeling for either 2PM or single photon techniques in rats.

Comparison with conventional microscopes

To evaluate the performance of cScope in vivo, we first compared cortical dynamics recorded using this macroscope in anesthetized rats, with dynamics recorded using a conventional widefield epifluorescence microscope similar to those used in previous studies (Ratzlaff and Grinvald 1991). Animals were anesthetized using 1% isoflurane in air and placed in a restraint apparatus (see methods for details). Imaging with both devices revealed slow frequency (<1 Hz) whole field oscillations across the cortex in GCaMP6f transgenic rats (Figure S5A-S5C). The magnitude and frequency of these oscillations was quantitatively similar across the two microscopes. Next, we performed the retinotopic mapping procedure described above and compared the maps of visual cortex generated using cScope and the conventional scope (Figure S5D). Both imaging procedures yielded maps of the primary visual cortex with similar contrast to noise (Figure S5E-S5F). Together, these results suggest that the head mounted scope captures similar dynamics and response amplitude compared with conventional widefield microscopes.

Effect of head mounted scope on spontaneous behavior

To evaluate the effect of the weight of cScope on motor activity and social interactions we recorded cortical dynamics and behavioral video in an open field environment. Implanted rats were transferred to a 0.5 by 0.5 m recording arena and cScope was attached to the animal's head. Although it was their first experience carrying the device, rats adapted to the weight and bulk of cScope within the first few minutes after attachments. The animal readily explored its new environment and displayed a number of natural behaviors including moving around the arena, approaching its cage mate, nose touch, grooming, feeding, standing on their hind feet, sniffing and whisking (Deschênes et al., 2012). During navigation, grooming and feeding the imaging field was remarkable stable and we did not observe a significant effect on the natural behavior of the animal due to the mass and bulk of cScope (Movie S2).

Evaluation of hemodynamic correction

Fluctuations in brightness observed of GCaMP6f labeled neurons are typically caused by multiple effects: 1) changes in GCaMP6f fluorescence efficiency due to free calcium concentration, and 2) differences in the absorption of excited or emitted light due to changes in the surrounding tissue, such as increased blood flow (Ma et al., 2016). To control for the influence of hemodynamics on the recorded GCaMP6f signal, images were acquired at either 30 Hz or 60 Hz with a stroboscopic illumination pattern in which 480 nm and 530 nm LED illumination were interleaved and synchronized with camera frame acquisition (Bouchard et al., 2009, Figure 6A-6B). This effectively reduced our imaging frame rate to 15 Hz and 30 Hz respectively, but allowed us to estimate the change in fluorescence signal due to hemodynamics. Correction was achieved by applying a divisive normalization scheme that has been previously described (Ma et al., 2016; Kramer and Pearstein 1979; Figure S6; Figure S7; see methods).

To evaluate the performance of our hemodynamic correction algorithm we examined the effect of correction on four artifacts which are produced by changes in blood flow. First, we examined the response of the visual cortex during a 2-second long stimulus presented to the contralateral visual field (Figure 6C-6D; see methods). Before correction, the GCaMP6f

fluorescence signal begins to decline well before the termination of the visual stimulus and then drops below baseline for several seconds before recovery (Figure 6C, blue line). The time course of this decline and recovery mirror the dynamics observed with 530 nm illumination (Figure 6C, green line). After correction the GCaMP fluorescence signal remains elevated for the duration of the stimulus and then decays to baseline (Figure 6C, black line). Next we examined the effect of hemodynamic correction on the visibility of surface vasculature in the spatial maps of GCaMP activation (Figure 6D). As expected, surface vasculature produced a significant spatially localized reduction in GCaMP fluorescence during the hemodynamic response (Figure 6D). Hemodynamic correction removes the pattern of vasculature from the spatial map of activity. We also examined the effect of correction on slow timescale visible changes in the vasculature that were associated with the beginning of an imaging session during behavior. Prior to correction GCaMP fluorescence increased over the first ten minutes of the imaging session, corresponding to a period of vasoconstriction. Correction dramatically reduced the slow timescale changes from the GCaMP fluorescence signal (Figure S7C). Finally, hemodynamic correction procedure was effective at reducing the influence the cardiac cycle on GCaMP fluorescence. A well documented artifact observed during widefield imaging is an oscillating signal produced by heartbeat of the animal (pulse; for example, see Shoham et al., 1999). Indeed, before applying the hemodynamic correction procedure, there was a significant modulation of the signal intensity recorded at 480 nm in the 5–8 Hz range (Figure S7A,S7D). After application of divisive normalization procedure, the power in the pulse range was significantly reduced (Figure S7D-S7E). Together, these results suggest that, consistent with previous work (Ma et al., 2016), the divisive normalization strategy for hemodynamic correction used by cScope was effective at reducing the contamination of the GCaMP signal by known hemodynamic artifacts.

Imaging global brain dynamics during behavior

We next sought to evaluate whether spatio-temporal patterns of activity related to behavior could be detected during a decision-making task. We reasoned that evidence-based decision-making tasks would provide a useful context to evaluate the performance of the mesoscale imaging in transgenic rats with cScope. While evidence-based decision-making tasks are thought to involve neural dynamics across multiple brain regions, most previous studies in animal subjects have focused on the dynamics of single neurons. More recently, 2PM calcium imaging has allowed simultaneous recordings of groups of neurons from a single region (Morcos et al., 2016; Scott et al., 2017), however the mesoscale dynamics remain unexplored. Therefore, it will be useful to complement cellular resolution electrophysiological and imaging studies with large scale recording that allow multiple regions to be observed simultaneously.

We trained THY1-GCaMP6f-7 rats (n=2) to perform a pulse-based visual accumulation of evidence task that we previously developed (Scott et al., 2015; Figure 7A, 7B). In this task subjects initiate a behavioral trial by inserting their nose into the center port of an operant training chamber. Subjects maintain their noise position while a sequence of brief flashes (10 ms) are presented from a left and a right LED (up to eight on each side). An auditory “go” cue indicates that they are free to orient to a left or right side nose port to obtain a water

reward. On each trial the timing and number of flashes is randomly determined, and subjects are rewarded for orienting to the side with the greater number of flashes. In a previous study we determined that rats solve this task using an accumulation process in which they combine evidence from early and late flashes to make their decision (Scott et al., 2015). The performance of transgenic, implanted rats was similar to wide-type rats (Figure 7C).

Rats were implanted with the cranial window (8mm by 4mm) and headplate assembly centered over a point approximately 4mm posterior and 2.75 mm to the right of Bregma (Figure 7D). Estimates based on stereotaxic coordinates suggested that a craniotomy of this size and position would allow optical access to primary and secondary visual cortex (V), parietal association cortex (P), somatosensory cortex (S), motor cortex (M), and retrosplenial cortex (R) (Paxinos and Watson 1998).

After recovery rats, rats were transferred to the imaging setup where we recorded cortical dynamics during the accumulation task. Frame-to-frame displacements in the AP and ML dimensions were less than one pixel, small enough to be effectively corrected offline by commonly used software (Figure S6F).

Next we examined the cortical response to individual flashes (Figure 7E-G, Figure S8, Movie S3). In this task the flashes are separated in time by a minimum of 250 ms allowing us to record the transient response to individual flashes without contamination from other stimuli. During the cue period both left and right flashes produced activation of multiple portions of the right V1 and V2. These patterns were consistent across imaging sessions and were similar across rats. Activation was strongest for flashes presented on the contralateral hemifield. These observations are consistent with previous cellular resolution imaging experiments during evidence accumulation that show transient activation of visual areas to visual evidence (Scott et al., 2017).

Next we examined how cortical activity patterns changed throughout a behavioral trial (Figure 8, Movie S4 and S5). On average, there was a reduction of GCaMP6f fluorescence throughout the entire FOV cue presentation period of the trial (Figure 8B,8C; Movie S4). This decay was particularly strong in the more anterior part of the FOV, corresponding to portions of the Motor and Somatosensory cortices. The opposite pattern of activation was evident during the response period of the task in which the animal oriented to the left or right reward port (Figure 8E, 8F lower panels; Movie S5). Visual cortical regions were most active during the cue period (Figure 8B,8C, 8E upper left panel) and different portions of visual cortex exhibited different temporal dynamics (Figure 8E upper right panel). The observed pattern in occipital and parietal cortex is similar to the dynamics observed with cellular resolution calcium imaging experiments during pulse-based accumulation tasks (Scott et al., 2017).

Finally, we analyzed how the responses at each position (pixel) differed across trial types (see methods). The mesoscale dynamics during the cue and response period were modulated by behavioral choice and stimulus identity (Figure 8F). During the cue period, stimulus identity could be inferred based on the activity of individual pixels within the visual cortical regions (Figure 8F upper panels) while during the response period behavioral choice could

be predicted by activity in parietal regions (Figure 8F lower panels). Together, these data are consistent with the model that multiple brain regions are recruited during complex behavioral tasks and demonstrate that cScope can provide precise spatio-temporal maps of cortical dynamics during behavior. These maps suggest potential new targets circuit level manipulation or cellular resolution recording studies.

Discussion

Here we report the development of a head mounted widefield macroscope capable of imaging a 7.8mm by 4mm FOV in freely moving animals. We also report the creation of strains of transgenic rats that express the genetically encoded calcium sensor GCaMP6f in the neurons of the neocortex and other forebrain regions. We demonstrate that these technologies can be combined to image calcium dynamics across large tracts of the forebrain in rats during decision- making navigation and social behavior. Our results extend the emerging field of head mounted microscopes into the mesoscale domain and provide a novel avenue to characterize global brain dynamics during natural behavior.

Comparison with other methods

Widefield microscopes for in vivo imaging at the mesoscale are typically based on a tandem lens design, and a scientific grade camera, often CMOS (Ratzlaff and Grinvald 1991). These systems offer large FOV, moderate NA (0.2 to 0.3) and high frame rate (>30Hz). Due to the size and weight of these devices, imaging in awake animals requires head restraint. A number of techniques have been developed, including virtual reality and voluntary head restraint, that provide the stability necessary for in vivo imaging while allowing the animal to express a wide range of behavior. However, there are a number of behaviors that have not been demonstrated with existing systems for head restraint, most notably sleep, social interaction and real world navigation. The key advantage of cScope is the ability to record neural dynamics without the need for head restraint with performance comparable to conventional widefield systems. In addition, cScope has two advantages over conventional widefield imaging systems. First cScope is simple to implement, less expensive and requires less equipment than conventional systems, therefore easier to parallelize for high-throughput behavioral facilities. Second the system has built-in light shielding facilitating experiments in which neural dynamics will be recorded during visual stimulation.

Head mounted microscopes have previously been developed for fluorescence calcium imaging and have been used to record spontaneous and sensory evoked responses in freely moving animals. However, these microscopes are designed for cellular resolution imaging and the largest FOV demonstrated with these microscope is small (<1 mm^2) compared with conventional widefield systems. Ferezou and colleagues developed a fiber-based microscope that enabled widefield fluorescence imaging of voltage sensitive dyes (Ferezou et al., 2006; Ferezou et al., 2007). While this device enabled measurements over a 2 by 2 mm field of view, it lacked the ability to perform hemodynamic correction. Moreover, because the size of the FOV was determined by the number of optical fibers implanted, further increasing the FOV of the fiberscope to the size offered by cScope would have resulted in a thick cable that could restrict movements of the animal. cScope brings the power of table top microscopes to

the head mounted domain allowing an area more than an order of magnitude larger than previous studies to be imaged in freely moving animals. This allows an experimenter to measure dynamics across multiple brain regions simultaneously during behavior. The FOV (>30mm^2) provided by cScope is large enough to contain multiple sensory, motor and association areas. Moreover, cScope offers the ability to simultaneously record fluorescence and intrinsic signals, which was not available in previous head mounted microscopes.

Interpretation of the widefield calcium signal

Care should be applied to the interpretation of signals obtained with cScope, and indeed any other widefield imaging system. One factor to be considered is the source of the calcium dependent fluctuations in GCaMP fluorescence level. Like previously reported Thy1-GCaMP mouse lines (for example Dana et al., 2014), the transgenic rats we developed exhibit widespread cortical labeling. Since the GCaMP molecule is free to diffuse through the axons, dendrites and somata of labeled neurons, fluorescence changes from any one pixel could reflect calcium levels in local layer 2/3 neurons, apical dendrites of deeper neurons or the axons of long range projections. These caveats are not unique to the system we present here, but are common factors effecting the interpretation of widefield imaging experiments.

A second consideration is that no method for hemodynamic correction completely corrects for the contamination of the GCaMP signal from changes in blood volume and oxygenation levels. The approach taken by cScope, which uses illumination near the peak emission wavelength of GCaMP, is widely used (Ma et al., 2016; Wekselblatt et al., 2016). However, because in our system the path taken by the blue light and green light are different, because blue light is scattered more than green light and because blue light is more strongly modulated by changes in the oxygenation level of blood, this correction cannot completely remove contamination due to the hemodynamic response. Improvements to the correction procedure may be obtained by the use of three color stroboscopic illumination (Ma et al., 2016) or the use of ultraviolet illumination at the calcium independent excitation wavelength of GCaMP (Allen et al., 2017). Nevertheless, the correction procedure we describe is sufficient to detect spatiotemporal dynamics similar to those recorded using cellular resolution imaging techniques and should be sufficient to identify new regions recruited during complex behavior.

Technological outlook and other applications

The two technologies we report here, used in combination or alone, offer a variety of experimental opportunities. As we demonstrated (Figure 5E-5F; Figure S4A-S4B; Movie S1), transgenic strains exhibit strong enough expression to allow for cellular resolution imaging. A number of techniques have been developed to allow cellular resolution imaging during behavior including voluntary head restraint (Scott et al., 2013), head mounted two photon microscopes (Helmchen et al., 2001; Sawinski et al., 2009; Zong et al., 2017) and head mounted single photon endoscopes (Ghosh et al., 2011; Cai et al., 2016). Transgenics offer stable expression over time and consistent expression across space, and have been popular for cellular resolution imaging in mice (Madisen et al., 2015).

In addition, some researchers may be interested in the use of transgenics for conventional widefield imaging in order to characterize the topographic arrangement of sensory systems. Wachowiak and colleagues previously used widefield imaging combined with calcium-sensitive dyes to characterize the functional organization of the olfactory bulb (Verhagen et al., 2007; Wesson et al., 2008; Carey et al., 2009). The transgenic rats we have developed provide an alternative to indicator dyes or viral delivery of genetically encoded indicators. Widefield imaging using GCaMP transgenic mice is widely used for characterizing the boundaries of secondary visual areas (Andermann et al., 2011; Marshel et al., 2011; Zhuang et al., 2017). Previous functional maps of visual areas have been produced for rats using electrophysiology (Espinoza and Thomas 1983) but GCaMP6f expressing transgenics will enable the generation of high resolution, high signal-to-noise maps and offer more direct comparison to maps produced in mice.

cScope also has potential for applications beyond use in transgenic rats. cScope could be used in wild type rats in which subpopulations of neurons are labelled with GCaMP using newly developed viral labeling techniques to express protein-based indicators in a projection specific or cell-type specific manner (Tervo et al., 2016; Dimidschstein et al., 2016). In addition, cScope could be used to record brain dynamics in other species. Although the weight is greater than that typically used for mouse, one potential avenue would be to develop a system with custom optics to reduce the size and weight of the microscope. Another possibility would be to apply cScope to larger animals, for example, the recent development of GCaMP-expressing transgenic marmosets (Park et al., 2016) make this an interesting opportunity.

cScope is not limited to measurement of neuronal calcium signals. While, in this study, we measured reflectance at 530 nm in order to correct for the effect of changes in blood flow on our measurement of GCaMP fluorescence, the hemodynamic response itself is a signal of interest, either as a proxy for neural activity, or as an indication of blood flow and metabolic activity. Another potential application of cScope would be to examine the relationship between hemodynamics and neural activity. While during passive sensory stimulation, the hemodynamic response is thought to follow increases in activity, it has been hypothesized that during behavior, increases blood flow may precede activity and serve a neuromodulatory function (Moore and Cao, 2008). Finally, modification of the LED wavelength, excitation and emission filters could allow imaging of voltage probes or other sensors.

Used in combination, the two technologies we developed offer a number of applications. Rats are adept at learning complex behaviors, and therefore popular as subjects for the investigation of the neural basis of decision-making. Widefield imaging would allow large swaths of cortex to be surveyed and used to target for either tetrode recording or cellular resolution imaging. In addition, these techniques offer a unique opportunity for studying mesoscopic dynamics during navigation, sleep or social interactions. For example, combining our system with prism technology (Low et al., 2014) could be a particularly interesting approach to image the of entorhinal cortex during 2D navigation.

Conclusion

Techniques for head restraint have been developed allowing in vivo functional imaging during sophisticated behaviors using conventional single photon and multi-photon imaging systems (Dombeck et al., 2007; Scott et al., 2013). However, head mounted microscopes offer the ability to record during a wider range of behaviors and require fewer modifications to existing behavioral paradigms. While previous head mounted fluorescent microscopes offer only a limited FOV, the system we describe here offers the ability to record dynamics across multiple brain regions. We anticipate that these technologies will provide new insight into the interactions between brain regions during complex behavior.

STAR Methods

Contact for Reagent and Resource Sharing

Further information and requests for reagents may be directed to and will be fulfilled by the Lead Contact, Dr. David Tank (dwtank@princeton.edu).

Experimental Model and Subject Details

Animal use procedures were approved by the Princeton University Institutional Animal Care and Use Committee (IACUC; Protocol #1837) and carried out in accordance with National Institutes of Health standards.

Production of transgenic rats

The Thy1 transgenic construct contained 4170 bp of the Thy1 gene enhancer/promoter region and 2130 bp of its 3' UTR region. The GCaMP6f –WPRE-bGH PA transgene was inserted into the Thy1 construct between the start codon and the XhoI site. The full insert was isolated and microinjected into Long-Evan rat embryos using standard techniques for pronuclear injection. The F0 rats were genotyped by PCR using primers in the GCaMP6f (5'- CATCAGTGCAGCAGAGCTTC-3') and in the WPRE (5' CAGCGTATCCACATAGCGTA-3') portions of the transgene (a 248 bp PCR product is expected for transgenic rats). Differences in expression observed using the Thy1-based approach are thought to arise from differences in the local regulatory environment around transgene integration sites.

Histology and confocal imaging

Animals were transcardially perfused with 4% paraformaldehyde in PBS. The brain was removed from the skull and post-fixed in 4% paraformaldehyde in PBS at 4^{o}C overnight and up to 1 week. Tissue sections (40–80 μm) were cut with a vibrating microtome (Leica). Sections were incubated at room temperature in PBS containing 10% bovine serum albumin and 0.5% triton 100 for 1 hour. Then transferred to PBS containing 5% bovine serum albumin, 0.4% triton 100, and with primary antibodies (anti-NeuN and anti-GFP) in blocking solution overnight at 4^{o}C overnight. This was followed by 3 washes in PBS and incubation in secondary antibodies (Alexa Fluor 488 goat anti-mouse IgG2 and Alexa Fluor 568 goat anti-mouse IgG1, 1:500 in PBS containing 5% bovine serum albumin, 0.4% triton 100) in blocking solution, and mounted on glass slides with liquid mounting medium

(Fluormount-G, ThermoFisher Scientific). Images were acquired using a Scanning confocal microscope Leica SP8.

To characterize the variability in transgene expression four rats from each line were perfused, histological sections containing the hippocampus were generated and imaged using a confocal microscope. Next we measured the average brightness of 100 different somata within the CA1 pyramidal cell layer. This approach was taken to allow direct comparison to previous results in Thy-1 GCaMP6 mice (Dana et al., 2014) Care was taken to insure that the histological and imaging parameters were identical across individual animals.

Two-photon imaging

Animals were imaged using a custom built two-photon microscope with conventional optics. The objective was a 16X water immersion objective (16X Nikon CFI LWD Plan Fluorite Objective, 0.80 NA). The excitation wavelength (Coherent, Chameleon) was 920nm. Imaging was performed in isoflurane anesthetized animals (1% in oxygen). Mosaic images were obtained using less than 250 mW average power and produced by stitching together individual fields of view using ImageJ. Spontaneous and stimulus evoked dynamics were recorded 200 microns below the cortical surface with an average power less than 105 mW. Brief (10ms) visual flashes from a blue (480 nm wavelength) LED were produced using a Master 8 controller. ROIs corresponding to active neurons were identified by CNMF (in Figure S4A as described in Pnevmatikakis, et al., 2016) or by manual identification of pixels based on morphology (in Figure S4B).

Animal surgery

Subjects were male and female THY-1 GCaMP6f rats aged 3 −12 months. Aseptic techniques were used throughout the surgical procedure. Implants and surgical tools were sterilized using an autoclave. Rats were anesthetized with isoflurane (1–2% in oxygen) and placed in a stereotaxic apparatus (David Kopf Instruments). A midline incision was made in the scalp and the skin was retracted exposing the skull. After removal of soft tissue from the dorsal surface of the skull, the perimeter of a rectangular portion of skull was removed by drilling creating a rectangular bone plug that could be removed with forceps. Large (8mm by 8mm) and small (8mm by 4mm) sized cranial windows were produced. Coordinates for the vertices of each of the different sized rectangular windows are listed in the table below (Table 1). Since the 8 by 8 mm cranial window spanned the midline, care was taken not to rupture the sagittal sinus during drilling or removal of the bone. Our approach was based on a technique developed for microprism implantation in mice (Low et al., 2014). Two rectangular windows from 8 mm long and 3.5 mm wide were drilled out. The bone plugs were left in place. Then the remaining 8mm by 1mm strip of bone was thinned down until it was flexible and transparent. Fragments of bone which lay over the cortex could be removed using forceps while fragments over the sagittal sinus were left in place. After thinning of the midline bone and removal of fragments, the two 3.5 by 8mm bone plugs on either side of the midline were removed.

After removal of the bone plugs the craniotomy was flushed with sterile saline to remove debris and blood. The dura was left intact unless removal of the bone plug caused partial tearing of the dura, or blood adhered to the dura compromising the optical quality of the signal. In either of these cases the dura was removed. Depending on the craniotomy size, one of two optical windows were then implanted: 8mm by 4 mm by 3mm for small craniotomies; 8mm by 8mm by 3mm for large craniotomies (obtained from Tower Optical). The windows were placed over the cortical surface and gentle pressure was applied until the surface had depressed roughly 200 microns below its original height. Vetbond was used at the margins of the window to secure the window to bone at the perimeter of the craniotomy. Dental Acrylic meta bond was then added to reinforce the bond. Once the window was firmly attached, the titanium ring was bonded to the skull centered over the craniotomy. Care was taken to ensure that the head plate lay parallel to the imaging surface of the glass and implanted at a height that would ensure the glass face of cScope made contact with the glass cranial window.

Comparison of conventional microscope and cScope

The conventional scope consisted of back-to-back objective system (Ratzlaff and Grinvald, 1991), a 1x objective lens and a 1.6x objective (Leica M-series) connected through a large filter box holding a dichroic mirror and emission filter (THT-microscope, Scimedia Ltd, Costa Mesa, CA, USA). The camera was a sCMOS optimos (Qimaging). In both head mounted and conventional systems the animal was anesthetized using either 1% isoflurane in oxygen (at 1L/min flow rate) or a cocktail of ketamine (100mg/kg) and xlyazine (10mg/kg). The animal's body temperature was maintained either using a thermal pad (Deltaphase Isothermal Pad). Visual stimuli were mapped using a custom script written in MATLAB which used the psychophysics toolbox 3 library (http://psychtoolbox.org). The flickering checkerboard stimulus pattern and the analysis scheme for generating retinotopic maps follows Juanvinett and colleagues (Juavinett et al., 2017; code available at https://snlc.github.io/ISI/).

To compare the sensitivity between the two microscopes we performed a measurement of the contrast to noise ratio, the contrast being the amplitude of the time-varying calcium signals detected by the system above background, with the noise being the variability in these signals when measuring them repeatedly. The following analysis was performed on the data. In the same animal, under identical anesthesia and stimulation conditions, we recorded the response to 15 sweeps of the visual field with a checkerboard stimulus. Three pixel locations were selected in the imaging field of view. To quantify the contrast to noise ratio for each pixel we identified the maximum of the average response across the 15 sweeps and took the average over a period beginning 25 points before the maximum and 25 points after the maximum. Next we identified the minimum of the average response and took the average over a period beginning 25 points before the minimum and 25 points after the minimum. The difference of these two values we defined as the contrast of our signal. Next we performed a high pass filter (by subtracting away the 50 point smoothed average signal) on the averaged response and computed the standard deviation. This we defined as the noise. Contrast to noise was defined as the ratio between the contrast and the noise.

Recording global brain dynamics

Illumination: The instantaneous power from the blue LED was up to 8.4mW. During 30hz stroboscopic illumination the Blue led was only on for 18ms out of 66ms which resulted in an average illumination power of 2.3mW over the imaging session. The instantaneous green LED was up to 0.360mW while the average power was up to 0.100mW (reduced due to stroboscopic illumination). The emission filter was a 50 nm bandpass filter centered at 525 nm and the excitation filter was a 40 nm bandpass filter centered at 470 nm.

Temperature Changes: The normal operating temperature of the rat dorsal neocortex is below the core body temperature of 37C and ranges from 34.8–36.8C (Franken et al., 1992). As demonstrated by the work of Kalmbach and Waters (Kalmbach and Waters 2012), craniotomies in rodents induce changes to the baseline temperature of the underlying brain tissue. In particular, the surface temperature is slightly reduced relative to pre-craniotomy. To directly examine temperature in our rats and how this was affected by microscope attachment and LED illumination, we implanted a thermocouple in a channel on the underside of the cranial window on two isoflurane anesthetized rats. Consistent with the work of Franken et al., and Kalmbach et al, we found that the temperature at the cortical surface of our implant, without the microscope attached, was 33.8–34.2C. Note that cortical temperature measurements conducted under isoflurane anesthesia are approximately 1C cooler than in awake animals (Kalmbach and Waters, 2012). After attachment of cScope, the cortical surface temperature stabilized in a few tens of seconds to a slightly reduced value within half a degree of that prior to the addition of the microscope. This is probably due to the greater thermal transport of microscope's glass objective contacting the cranial window relative to air. Powering up cScope's LEDs caused an increase of roughly 0.7C of the cortical surface over the first 15–20 minutes, which then plateaued. These modest increases in temperature correlate with the vasoconstriction we observe over the first several minutes of an imaging session. This vasoconstriction provided us with a means to assess the effectiveness of our hemodynamic correction (Figure S7). In our experiments with anesthetized rats we did not observe cortical temperature during imaging over 34.6C or below 33.3C, implying cortical temperatures in awake rats were in the 34.3–35.6C range.

Spontaneous Behavior: Rats were allowed to recover for 7 days after surgery before behavioral experiments. During recovery they were housed with cage mates in a facility on a reversed light schedule. On the day of experiment both rats were transferred to a 0.5 by 0.5 meter arena. The focal plane of cScope was preset to the bottom of cranial window. To that end a jig was assembled that incorporates a Siemens Star target located below a 3mm glass window over which cScope was placed. The camera mounted on a translating arm was tuned for best focus and secured in position. cScope was then transferred onto the head of one of the animals. The 2 meter cable connecting the LEDs and cScope camera to the power and data acquisition device was suspended over the center of the arena with enough slack so that the rat could move freely. Behavior was recorded using a USB camera. Behavioral video and cScope images were synchronized using freely available acquisition software (Miniscope DAQ software; Miniscope project, http://miniscope.org/).)

Accumulation of evidence: Three adult male rats were trained in an automated high-throughput facility as previously described (Scott et al., 2015). Once rats learned the task (>60% performance) they were implanted with an 8 by 4 mm cranial window and head plate as described above. After one week recovery, rats were anesthetized using isoflurane (1% in oxygen) and the illumination collar was mounted on their head plate. cScope was attached and the focus was adjusted to match the surface vasculature. The illumination collar remained in place for the duration of remaining of the experiment (typically 1–4 weeks). The animals were imaged daily for 30–90 minutes while they performed the accumulation task. At the start of each imaging session cScope was inserted in the illumination collar, secured with a set screw and removed after completion of the session. A dust cap was placed on the illumination collar between sessions to protect the LEDs and cranial window while the rat was returned to its home cage (Figure S3).

Behavioral software (Bcontol) was used to control the timing of trial events, such as the visual flashes, auditory “go” signal and reward, and to record the animals’ responses during the imaging session. cScope images were recorded using Miniscope DAQ software as described above. Clock synchronization between the imaging files and the behavioral files were accomplished by controlled disruption of LED power which produced “blank frames” at specific times. At the completion of each trial the behavioral control system sent a TTL pulse to the microcontroller responsible for alternating the power supply to the LEDs. This TTL pulse temporarily closed a gate between the supply and the LED. Blank frames could then be matched with the timings of the TTL pulses recorded in the behavioral files in order to synchronize the behavioral clock and the miniscope system clock.

Analysis of widefield data

After acquisition, image files were processed using custom scripts in MATLAB. Image analysis pipeline consisted of the following stages:

1) The images from individual .avi files were combined into a single 3D matrix

2) The 3D matrix was down sampled in the spatial domain by binning 2 by 2 pixel regions and by cropping the field of view to remove the regions outside of the cranial window.

3) The imaging timestamp file was used to identify lost frames (see Methods S1 – Timestamp correction) and the system clock file was corrected.

4) The 3D matrix was split into two 3D matrices, one with frames acquired at 480 nm illumination and another at 530 nm illumination. Each matrix was then motion corrected using NoRMCorre. (https://github.com/simonsfoundation/NoRMCorre) and down sampled again in the spatial domain by binning 2 by 2 pixel regions.

5) I/Io for was computed for each pixel where I was a vector of the intensity values of that pixel on each frame and Io was the mean intensity across the imaging session.

6) Hemodynamic correction for each pixel in the 480 nm matrix was performed to obtain the estimated GCaMP fluorescence changes (see Hemodynamic correction below).

Note that in the results section and figures the term “pixel” corresponds to the region obtained after step 6, therefore it is equivalent to a 4-by-4 pixel area in the original camera image.

Hemodynamic correction

To correct for fluorescence intensity changes caused by changes in the optical properties of the tissue we used an approach previously described by Kramer and Pearstein (1979) and Ma et al., (2016). In this approach the changes in fluorescence intensity due to blood absorption are approximated by reflectance intensity changes at 530 nm and corrected using the following equation:

$$\frac{F}{F_0} = \frac{I^{480}/_0^{480}}{I^{530}/I_0^{530}}$$

where I^{480} is the recorded fluorescence signal, I^{530} is the corrected reflectance signal (see below), and F the level of fluorescence signal would be in the absence of varying absorption. However, at some pixel locations in the imaging window we observed reflections off the glass and metabond that significantly increased the baseline intensity values on frames recorded during 530 nm LED illumination. A consequence of these changes in baseline would lead us to underestimate I^{530}/Io^{530} and under correct for the hemodynamic response. Therefore, we assumed that for each pixel:

$$I_{meas} = I^{530} + \alpha$$

where α was an offset value produced by reflections. α was computed independently at each pixel and was allowed to vary over space, but was assumed to be static over time. Two different methods were used to identify α for each pixel.

Method #1: This method for computing α used the gradual intensity increase observed over the first 10 minutes after placement of cScope on the animal (Figure S6). We noticed a constriction of the vasculature across the imaging window after placement of cScope on the animal head. This constriction is consistent with known changes in vasodilation due to modest temperature changes (see above). In this approach α was defined as the value that minimized error according to the following equation:

$$error = \sqrt{\sum\left(\frac{I^{480}}{I_0^{480}} - \frac{I^{530}}{I_0^{530}}\right)^2}$$

Method #2: To identify α for each pixel we used the component of the signal modulated by the pulse (heartbeat), typically a regular oscillation between 5 and 8 Hz: For each imaging session the pulse frequency window (pulse window) was first determined by the user by examining the power spectrum density function on the 530 nm LED channel computed by the fast Fourier transform (Matlab function fft.m) and choosing the upper and lower bounds that framed the peak in the power spectrum at 5–8 Hz. Then α was defined as the value that minimized the power in the pulse window (pulse power) as defined by the following equation:

$$pulse\ power = \sqrt{\sum \left(Y - Y_{pred}\right)^2}$$

where Y was the fast Fourier transform on F/Fo and Y_{pred} was the "baseline" linear prediction (based on least squares regression) of Y in the pulse frequency based values of Y outside the pulse window. Results are shown in Figure S7D.

We found that both methods identified similar α values at each pixel and moreover we found that the α values determined by method #1 was effective both at reducing slow timescale fluctuations caused by vasoconstriction (Figure S7C) and at reducing the pulse power (Figure S7E). Figure S7D shows the results of hemodynamic correction using α values computed using method #2. All other figure panels containing GCaMP data with hemodynamic correction use method #1 for identifying the α values. In our imaging experiments α was at or close to 0 for most pixels (Figure 6D).

For some pixels, particularly those near the corners of the FOV where 480 nm illumination is low, we found that the best fit α did not correct for the hemodynamic response. Therefore, we excluded pixels from further analysis if the error for the best fit α exceeded a manually determined threshold (Figure S6E).

Classifier accuracy

We used the following algorithm to calculate the accuracy with which we could predict the choice of the animal (or stimulus identify) based on the activity of individual pixels. For each pixel we created two distributions, the activity of that pixel on right choice trials comprised one distribution and the activity of the pixel on left choice trials comprised the other. Next for each pixel, we found the threshold value that maximally separated these two distributions. Classifier accuracy was defined as the average between two values 1) proportion of values from the distribution of the greater mean that was greater than the threshold and 2) proportion of values from the distribution of the lesser mean that was less than the threshold.

Evaluation of hemodynamic correction

One GCaMP6f-line7 rat was implanted with an optical window over V1. After recovery the animal was anesthetized using a cocktail of ketamine and xylazine and placed in front of an LCD screen. A two-second long visual stimulus, alternating full field checkerboard, was

presented to the contralateral visual field. This stimulus was followed by a 10-second long iso- luminant screen, and this was repeated 180 times.

Supplemental methods for the fabrication and use of cScope

A detailed guide for cScope assembly and use is provided in supplementary material (Figure S2 and Methods S1). A full parts list, hardware designs, and software for control and analysis are available via the cScope GitHub repository (https://github.com/PrincetonUniversity/cScope). The .dwfx assembly file can be visualized using the online freely available viewer (https://viewer.autodesk.com). We provide a Matlab (Mathworks) routine to help quantify the parameters of the transformation to apply for image correction. Figure S1D bottom panel shows the result of the post-processing step applied to the grid image. This procedure was not applied to the in vivo imaging data we present in figures 7 and 8, however, it is useful if the experiment requires precise alignment with stereotaxic coordinates. Image acquisition software and other information related to the imaging camera can be obtained from the Miniscope project http://miniscope.org/

Supplementary Material

Refer to Web version on PubMed Central for supplementary material.

Acknowledgements

The authors would like to thank Krista Saufler (Princeton) for breeding of the transgenics. Lucas Pinto (Princeton) and Sue Ann Koay (Princeton) provided helpful discussions and contributed software related to processing widefield imaging data. Christine Constantinople (Princeton) and Klaus Osorio (Princeton) provided assistance with behavioral training and handling during the accumulation of evidence experiments. Rhino Nevers (Princeton), Yi Gu (Princeton) and Deepika Walpita (Janelia) assisted with histological preparation and analysis. Daniel Aharoni (UCLA) provided useful details related to the image acquisition system. The work was supported by NIH grant number U01NS090541 to C.D.B. and D.W.T., the Howard Hughes Medical Institute, the Bezos Center for Neural Circuit Dynamics (Princeton University) and the Simons Foundation (SCGB).

References

Ahrens MB, Li JM, Orger MB, Robson DN, Schier AF, Engert F and Portugues R, (2012). Brain-wide neuronal dynamics during motor adaptation in zebrafish. Nature 485, 471–477. [PubMed: 22622571]

Allen WE, Kauvar IV, Chen MZ, Richman EB, Yang SJ, Chan K, Gradinaru V, Deverman BE, Luo L and Deisseroth K, (2017). Global representations of goal-directed behavior in distinct cell types of mouse neocortex. Neuron 94(4), 891–907. [PubMed: 28521139]

Andermann ML, Kerlin AM, Roumis DK, Glickfeld LL, and Reid RC (2011). Functional specialization of mouse higher visual cortical areas. Neuron 72, 1025–1039. [PubMed: 22196337]

Aronov D and Tank DW (2014). Engagement of neural circuits underlying 2D spatial navigation in a rodent virtual reality system. Neuron 84, 442–456. [PubMed: 25374363]

Bonhoeffer T and Grinvald A, (1991) Iso-orientation domains in cat visual cortex are arranged in pinwheel-like patterns, Nature 353, 429–431 [PubMed: 1896085]

Bouchard MB, Chen BR, Burgess SA, and Hillman EM (2009). Ultra-fast multispectral optical imaging of cortical oxygenation, blood flow, and intracellular calcium dynamics. Opt. Express 17, 15670–15678. [PubMed: 19724566]

Cai DJ, Aharoni D, Shuman T, Shobe J, Biane J, Song W, Wei B, Veshkini M, La-Vu M, Lou J and Flores SE (2016). A shared neural ensemble links distinct contextual memories encoded close in time. Nature 534, 115–118. [PubMed: 27251287]

Carey RM, Verhagen JV, Wesson DW, Pírez N and Wachowiak M (2009). Temporal structure of receptor neuron input to the olfactory bulb imaged in behaving rats. Journal of Neurophysiology 101,1073–1088. [PubMed: 19091924]

Chen TW, Wardill TJ, Sun Y, Pulver SR, Renninger SL, Baohan A, Schreiter ER, Kerr RA, Orger MB, Jayaraman V and Looger LL (2013). Ultrasensitive fluorescent proteins for imaging neuronal activity. Nature 499, 295–300. [PubMed: 23868258]

Dana H, Chen TW, Hu A, Shields BC, Guo C, Looger LL, Kim DS and Svoboda K, (2014). Thy1-GCaMP6 transgenic mice for neuronal population imaging in vivo. PLoS One 9, e108697. [PubMed: 25250714]

Deschênes M, Moore J and Kleinfeld D (2012). Sniffing and whisking in rodents. Curr. Opin. Neurobiol 22, 243–250. [PubMed: 22177596]

Dimidschstein J, Chen Q, Tremblay R, Rogers SL, Saldi GA, Guo L, Xu Q, Liu R, Lu C, Chu J and Grimley JS (2016). A viral strategy for targeting and manipulating interneurons across vertebrate species. Nat Neurosci 19, 1743–1749. [PubMed: 27798629]

Espinoza SG, and Thomas HC (1983). Retinotopic organization of striate and extrastriate visual cortex in the hooded rat. Brain Res 272, 137–144. [PubMed: 6616189]

Feller MB, Wellis DP, Stellwagen D, Werblin FS, and Shatz CJ (1996). Requirement for cholinergic synaptic transmission in the propagation of spontaneous retinal waves. Science 272, 1182. [PubMed: 8638165]

Feng G, Mellor RH, Bernstein M, Keller-Peck C, Nguyen QT, Wallace M, Nerbonne JM, Lichtman JW and Sanes JR (2000). Imaging neuronal subsets in transgenic mice expressing multiple spectral variants of GFP. Neuron 28, 41–51 [PubMed: 11086982]

Ferezou I, Bolea S and Petersen CC (2006). Visualizing the cortical representation of whisker touch: voltage-sensitive dye imaging in freely moving mice. Neuron 50, 617–629. [PubMed: 16701211]

Ferezou I, Haiss F, Gentet LJ, Aronoff R, Weber B and Petersen CC (2007). Spatiotemporal dynamics of cortical sensorimotor integration in behaving mice. Neuron 56, 907–923. [PubMed: 18054865]

Franken P, Tobler I, & Borbély AA (1992). Sleep and waking have a major effect on the 24- hr rhythm of cortical temperature in the rat. Journal of Biological Rhythms 7(4), 341–352. [PubMed: 1286205]

Ghosh KK, Burns LD, Cocker ED, Nimmerjahn A, Ziv Y, El Gamal A and Schnitzer MJ (2011). Miniaturized integration of a fluorescence microscope. Nat. Methods 8, 871–878. [PubMed: 21909102]

Gias C, Hewson-Stoate N, Jones M, Johnston D, Mayhew JE and Coffey PJ (2005). Retinotopy within rat primary visual cortex using optical imaging. Neuroimage 24, 200–206. [PubMed: 15588611]

Grinvald A, Lieke E, Frostig RD, Gilbert CD and Wiesel TN (1986) Functional architecture of cortex revealed by optical imaging of intrinsic signals. Nature 324, 361 –364 [PubMed: 3785405]

Gu X, Olson EC, and Spitzer NC (1994). Spontaneous neuronal calcium spikes and waves during early differentiation. J Neurosci 14, 6325–6335. [PubMed: 7965039]

Helmchen F, Fee MS, Tank DW and Denk W (2001). A miniature head-mounted two- photon microscope: high-resolution brain imaging in freely moving animals. Neuron 31, 903–912. [PubMed: 11580892]

Juavinett AL, Nauhaus I, Garrett ME, Zhuang J, and Callaway EM (2017). Automated identification of mouse visual areas with intrinsic signal imaging. Nat. Protoc 12, 32–43. [PubMed: 27906169]

Kalmbach AS, & Waters J (2012). Brain surface temperature under a craniotomy. Journal of Neurophysiology 108(11), 3138–3146. [PubMed: 22972953]

Kramer RS, and Pearlstein RD (1979). Cerebral cortical microfluorometry at isosbestic wavelengths for correction of vascular artifact. Science 205, 693–696. [PubMed: 223243]

Kloosterman F, Davidson TJ, Gomperts SN, Layton SP, Hale G, Nguyen DP, Wilson MA (2009). Micro-drive Array for Chronic *in vivo* Recording: Drive Fabrication. J. Vis. Exp 26, e1094.

Liberti WA, III, Perkins LN, Leman DP, & Gardner TJ (2017). An open source, wireless capable miniature microscope system. Journal of Neural Engineering 14(4), 045001. [PubMed: 28514229]

Low RJ, Gu Y, and Tank DW (2014). Cellular resolution optical access to brain regions in fissures: imaging medial prefrontal cortex and grid cells in entorhinal cortex. Proc. Natl. Acad. Sci. USA 111, 18739–18744. [PubMed: 25503366]

Ma Y, Shaik MA, Kim SH, Kozberg MG, Thibodeaux DN, Zhao HT, Yu H, and Hillman EMC (2016). Wide-field optical mapping of neural activity and brain haemodynamics: considerations and novel approaches. Phil. Trans. R. Soc. B 371, 20150360. [PubMed: 27574312]

Madisen L, Garner AR, Shimaoka D, Chuong AS, Klapoetke NC, Li L, van der Bourg A, Niino Y, Egolf L, Monetti C and Gu H (2015). Transgenic mice for intersectional targeting of neural sensors and effectors with high specificity and performance. Neuron 85, 942–958. [PubMed: 25741722]

Marshel JH, Garrett ME, Nauhaus I, and Callaway EM (2011). Functional specialization of seven mouse visual cortical areas. Neuron 72, 1040–1054. [PubMed: 22196338]

Miao P, Zhang L, Li M, Zhang Y, Feng S, Wang Q and Thakor NV (2017). Chronic wide-field imaging of brain hemodynamics in behaving animals. Biomed. Opt. Express 8, 436–445. [PubMed: 28101429]

Moore CI and Cao R (2008). The hemo-neural hypothesis: on the role of blood flow in information processing. J Neurophysiol 99, 2035–2047. [PubMed: 17913979]

Morcos AS, and Harvey CD (2016). History-dependent variability in population dynamics during evidence accumulation in cortex. Nature Neuroscience 19(12), 1672. [PubMed: 27694990]

Murphy TH, Boyd JD, Bolaños F, Vanni MP, Silasi G, Haupt D, and LeDue JM (2016). High-throughput automated home-cage mesoscopic functional imaging of mouse cortex. Nature Communications 7, 11611.

Park JE, Zhang XF, Choi SH, Okahara J, Sasaki E and Silva AC (2016). Generation of transgenic marmosets expressing genetically encoded calcium indicators. Scientific Reports 6, 34931. [PubMed: 27725685]

Paxinos G, and Watson C (1998). A stereotaxic atlas of the rat brain. San Diego: Academic

Ratzlaff EH, and Grinvald A (1991). A tandem-lens epifluorescence macroscope: hundred- fold brightness advantage for wide-field imaging. J Neurosci Methods, 36, 127–137. [PubMed: 1905769]

Sawinski J, Wallace DJ, Greenberg DS, Grossmann S, Denk W, & Kerr JN (2009). Visually evoked activity in cortical cells imaged in freely moving animals. Proc. Natl. Acad. Sci. USA 106(46), 19557–19562. [PubMed: 19889973]

Scott BB, Brody CD, and Tank DW (2013). Cellular resolution functional imaging in behaving rats using voluntary head restraint. Neuron 80, 371–384. [PubMed: 24055015]

Scott BB, Constantinople CM, Erlich JC, Tank DW, and Brody CD (2015). Sources of noise during accumulation of evidence in unrestrained and voluntarily head-restrained rats. Elife 4, e11308. [PubMed: 26673896]

Scott BB, Constantinople CM, Akrami A, Hanks TD, Brody CD, and Tank DW (2017). Fronto-parietal cortical circuits encode accumulated evidence with a diversity of timescales. Neuron 95, 385–398. [PubMed: 28669543]

Shoham D, Glaser DE, Arieli A, Kenet T, Wijnbergen C, Toledo Y, Hildesheim R and Grinvald A (1999). Imaging cortical dynamics at high spatial and temporal resolution with novel blue voltage-sensitive dyes. Neuron 24, 791–802. [PubMed: 10624943]

Skocek O, Nöbauer T, Weilguny L, Traub FM, Xia CN, Molodtsov MI, Grama A, Yamagata M, Aharoni D, Cox DD and Golshani P (2018). High-speed volumetric imaging of neuronal activity in freely moving rodents. Nat. Methods 15, 429–432. [PubMed: 29736000]

Steinmetz NA, Buetfering C, Lecoq J, Lee CR, Peters AJ, Jacobs EA, Coen P, Ollerenshaw DR, Valley MT, de Vries SE and Garrett M, 2017 Aberrant cortical activity in multiple GCaMP6-expressing transgenic mouse lines. eNeuro 4(5), pp.ENEURO-0207.

Tervo DGR, Hwang BY, Viswanathan S, Gaj T, Lavzin M, Ritola KD, Lindo S, Michael S, Kuleshova E, Ojala D and Huang CC (2016). A designer AAV variant permits efficient retrograde access to projection neurons. Neuron 92, 372–382. [PubMed: 27720486]

Tian L, Hires SA, Mao T, Huber D, Chiappe ME, Chalasani SH, Petreanu L, Akerboom J, McKinney SA, Schreiter ER and Bargmann CI (2009). Imaging neural activity in worms, flies and mice with improved GCaMP calcium indicators. Nat. Methods 6, 875–881. [PubMed: 19898485]

Verhagen JV, Wesson DW, Netoff TI, White JA, and Wachowiak M (2007). Sniffing controls an adaptive filter of sensory input to the olfactory bulb. Nat. Neurosci 10, 631–639. [PubMed: 17450136]

Wekselblatt JB, Flister ED, Piscopo DM, and Niell CM (2016) Large-scale imaging of cortical dynamics during sensory perception and behavior, J Neurophysiol 115, 2852–66. [PubMed: 26912600]

Wesson DW, Carey RM, Verhagen JV, and Wachowiak M (2008). Rapid encoding and perception of novel odors in the rat. PLoS Biol 6(4), e82. [PubMed: 18399719]

Wong ROL, Chernjavsky A, Smith SJ, and Shatz CJ (1995). Early functional neural networks in the developing retina. Nature 374, 716–718. [PubMed: 7715725]

Yuste R, Nelson DA, Rubin WW, and Katz LC (1995). Neuronal domains in developing neocortex: mechanisms of coactivation. Neuron 14, 7–17. [PubMed: 7826643]

Yamamoto J and Wilson MA (2008). Large-scale chronically implantable precision motorized microdrive array for freely behaving animals. J Neurophysiol 100, 2430–2440. [PubMed: 18667539]

Zhuang J, Ng L, Williams D, Valley M, Li Y, Garrett M, and Waters J (2017). An extended retinotopic map of mouse cortex. eLife 6, e18372. [PubMed: 28059700]

Ziv Y and Ghosh KK (2015). Miniature microscopes for large-scale imaging of neuronal activity in freely behaving rodents, Curr Opin Neurobiol 32, 141–147. [PubMed: 25951292]

Zong W, Wu R, Li M, Hu Y, Li Y, Li J, Rong H, Wu H, Xu Y, Lu Y, Jia H, Fan M, Zhou Z, Zhang Y, Wang A, Chen L, Cheng H, (2017), Fast high-resolution miniature two-photon microscopy for brain imaging in freely behaving mice, Nat. Methods 14, 713–719. [PubMed: 28553965]

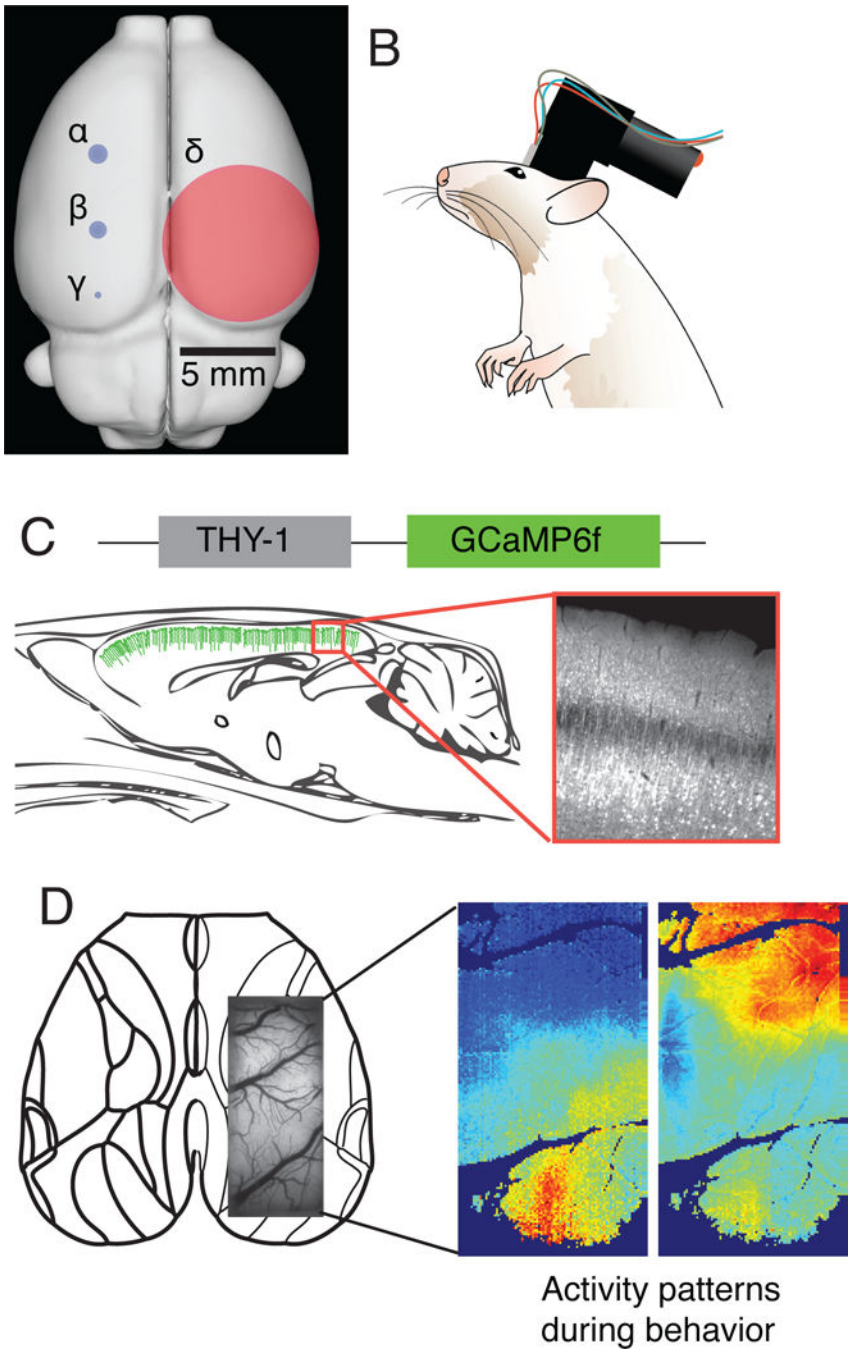

Figure 1.

Strategy for imaging mesoscale cortical dynamics during behavior A) Schematic of the rat brain showing the FOV for previously developed head mounted fluorescence microscopes (blue dots). α: Ghosh et al., 2011; α Miniscope.org; β; Zong et al., 2017. Indicated in pink is the FOV achieved in the present study. (B) Schematic of a rat wearing cScope. (C) The development of transgenic rats with dense neuronal GCaMP6f expression in neocortex facilitates imaging with cScope and may be used in cellular resolution two photon microscopy. (D) Schematic of anticipated results. Left panel: Wireframe illustration of a

dorsal view of rat cortex. Lines indicate area boundaries based on stereotaxic coordinates. An epifluorescence image of the rat brain is overlaid to indicated the relative size of the camera FOV attained in the current study. Right panels show cortical activation patterns at two different times. Red pixels indicated high levels of GCaMP fluorescence, blue pixels indicate low levels. This technique allows analysis of neural dynamics across multiple brain regions simultaneously in freely moving animals.

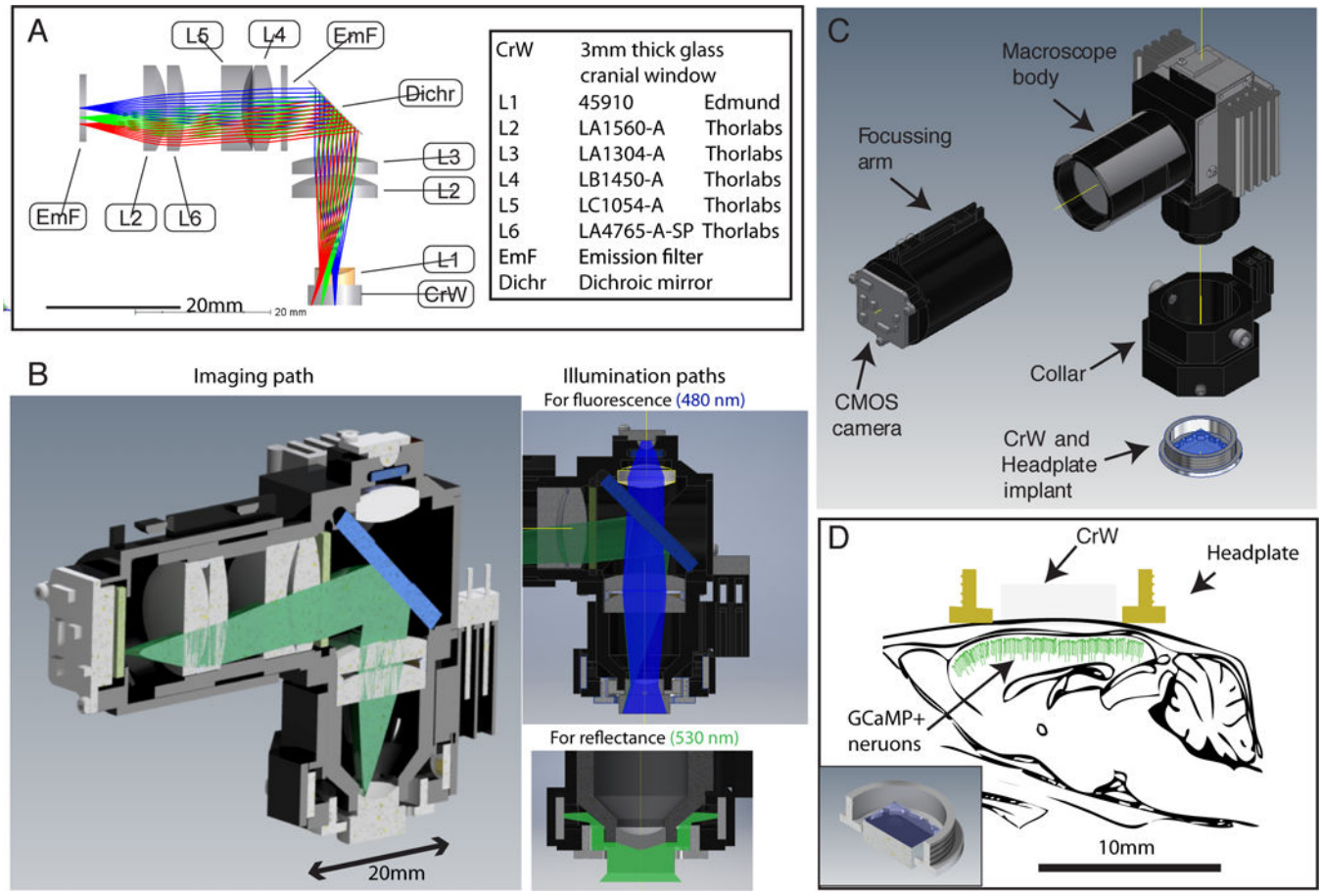

Figure 2.

Design of cScope, a head mounted cortical macroscope (A) Imaging path of cScope and list of the commercially available lenses used in the design. The elements below the folding dichroic mirror constitute the macroscope objective and includes a diverging lens (L1) in contact with the implanted glass window and a doublet of plano-convex lenses (L2/L3). Two plano-convex lenses are used instead of a single element to minimize the amount of spherical aberration generated. The four elements on the left of the mirror form the tube lens of the macroscope. The far left doublet (L6/L2) is focusing the light on the imaging sensor. The other doublet (L4/L5) reduces the overall aberrations of the macroscope. This is illustrated in the Seidel diagram of Figure S1 which shows the contribution of each surface to the five different third-order aberrations. (B) Section view of the macroscope assembly showing the imaging path (left). Cross-section views of the macroscope illustrating the illumination paths of the fluorescence and reflectance sources (right). (C) CAD design of the macroscope showing the four main parts of assembly. a. the head plate and 3mm thick glass window implant, b. a collar that screws on the head-plate and serves both as a structural component that holds the macroscope attached to the animal, and as the housing of the green light source used for reflectance imaging, c. the main part of the macroscope, holding all the optics as well as the fluorescent light source, and finally d. a focusing arm carrying the camera and which position is adjusted to focus on the brain surface. The complete part list, the CAD models of the parts, and the detailed guide for the macroscope assembly are given

in supplementary material including Figures S2 and S3. (D) Schematic cross section of the animal implant showing the rat brain, the glass window (to scale), and the titanium head plate.

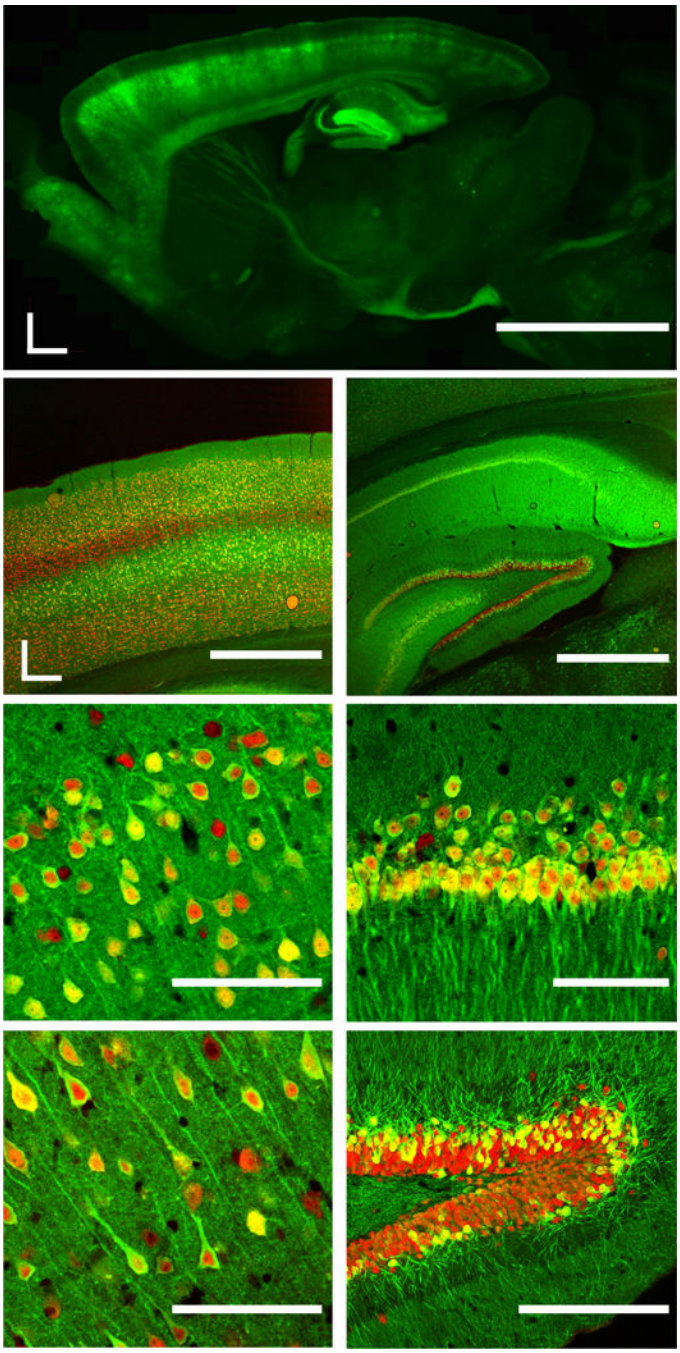

Figure 3.

Expression of GCaMP6f in neocortex and hippocampus of THy1 GCaMP6f-7 transgenic rats (A) Epifluorescence microscopy image of native GCaMP expression (green) in a parasagittal histological section from a Thy-1-GCaMP6f-7 rat. (B-G) Confocal microscopy images of histological sections labeled with antibodies against GFP (green, Alexa Fluor 488 conjugated) and NeuN (red, Alexa Fluor 568 conjugated). (B) GCaMP expression was observed throughout the cortical layers with NeuN+ GCaMP+ labeling of cell bodies in layer 2/3 (C) and layer 5 (D). (E) Significant levels of GCaMP was also observed in the

hippocampus, somatic labeling occurred in cells of the pyramidal layer of CA1 (F) and the granules cell layer of the dentate gurus (G). See also Figure S4.

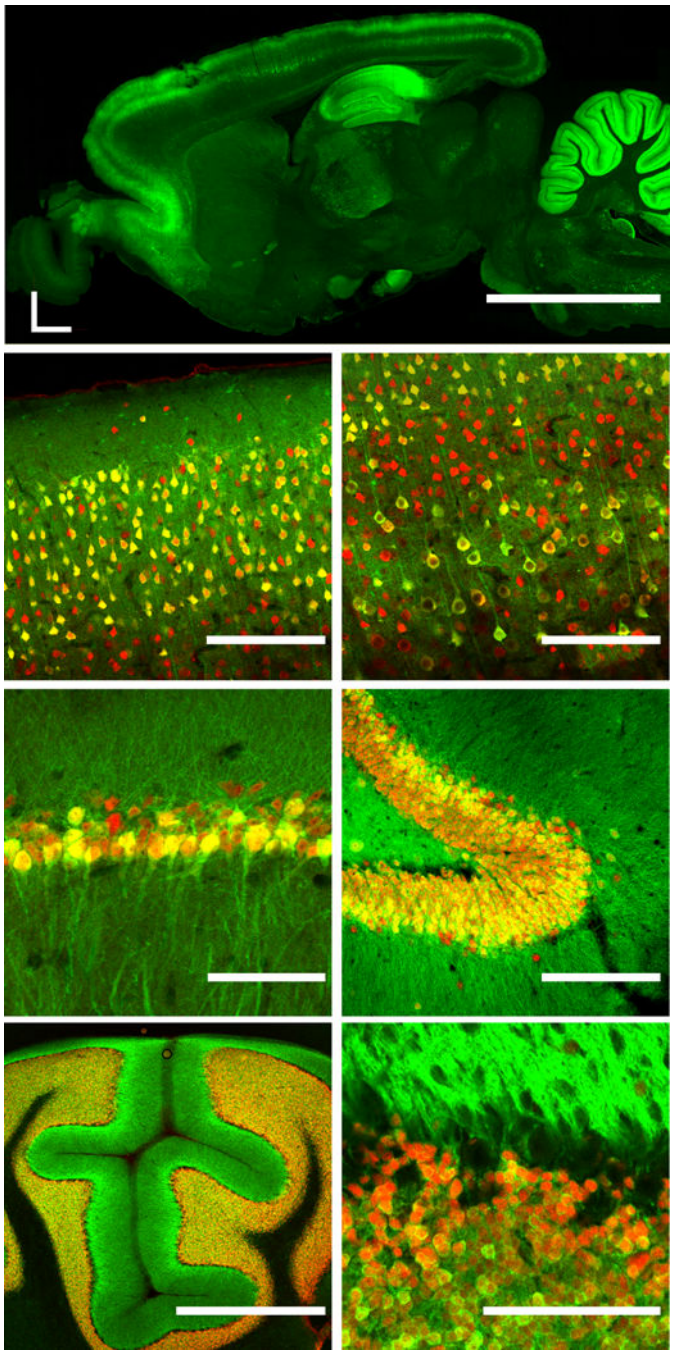

Figure 4.

Expression of GCaMP6f in neocortex, hippocampus and cerebellum of THy1 GCaMP6f-9 (A) Epifluorescence microscopy image of native GCaMP expression (green) in a parasagittal histological section from a Thy-1-GCaMP6f-9 rat. (B-D) Confocal microscopy images of histological sections labeled with antibodies against GFP (green, Alexa Fluor 488 conjugated) and NeuN (red, Alexa Fluor 568 conjugated). (B) GCaMP expression was observed in the expression in the somatic cytoplasm of NeuN positive neurons in layer 2/3 (left) and layer 5 (right). (C) GCaMP+, NeuN+ cell bodies in the pyramidal layer of CA1

(left) and the granule cell layer of the dentate gurus (right). (D) GCaMP labeling of granule cells in the cerebellum.

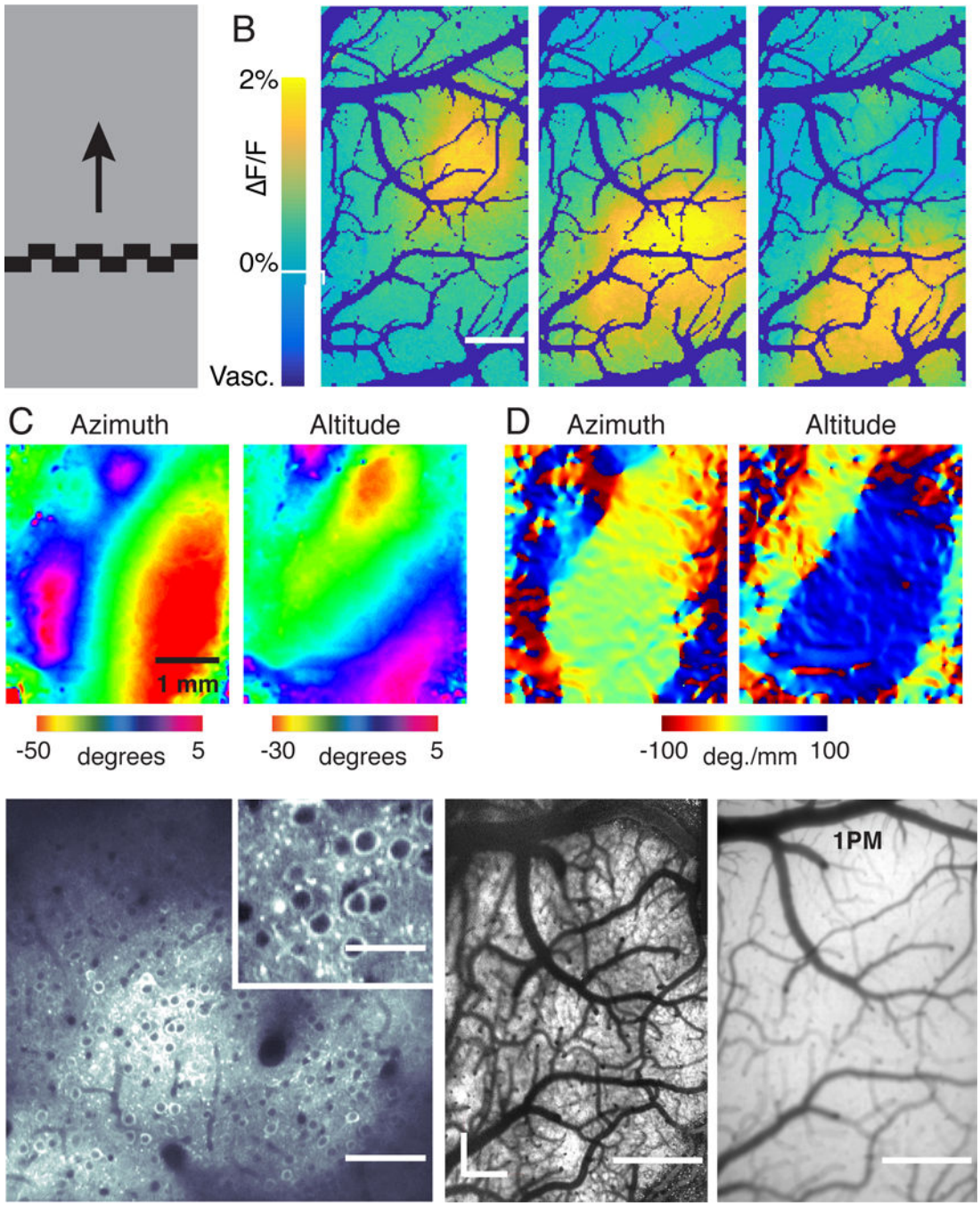

Figure 5.

Imaging GCaMP6f expression and calcium dynamics in vivo (A) Checkerboard visual stimulus used for retinotopic widefield mapping experiments. Arrow indicates the direction of movement of the upward drifting stimulus used to elicit the fluorescence dynamics shown in E. (B) Example of GCaMP6f fluorescent changes in a Thy1- GCaMP6f-7 rat as the checkerboard visual stimulus shown in panel A moves upward. The altitude of the stimulus relative to the visual equator of the rat is indicated at the top of each map. (C) Example Azimuth and Altitude maps produced by retinotopic mapping with the moving checkerboard

stimulus across the four cardinal directions. (D) Azimuth and altitude gradient maps computed from the maps in F reveal the borders of the primary visual area. See also Figure S5. (E) Two photon microscopy (2PM) image of GCaMP6f expression in neuronal cell bodies and neuropil in layer 2/3 of the intact brain from a Thy1-GCaMP6f-7 rat. (F) Large field of view obtained from mosaic 2PM imaging of GCAMP fluorescence in rat implanted with a large rectangular cranial window. (G) Field of view show in F imaged by single photon epifluorescence microscopy through the same cranial window.

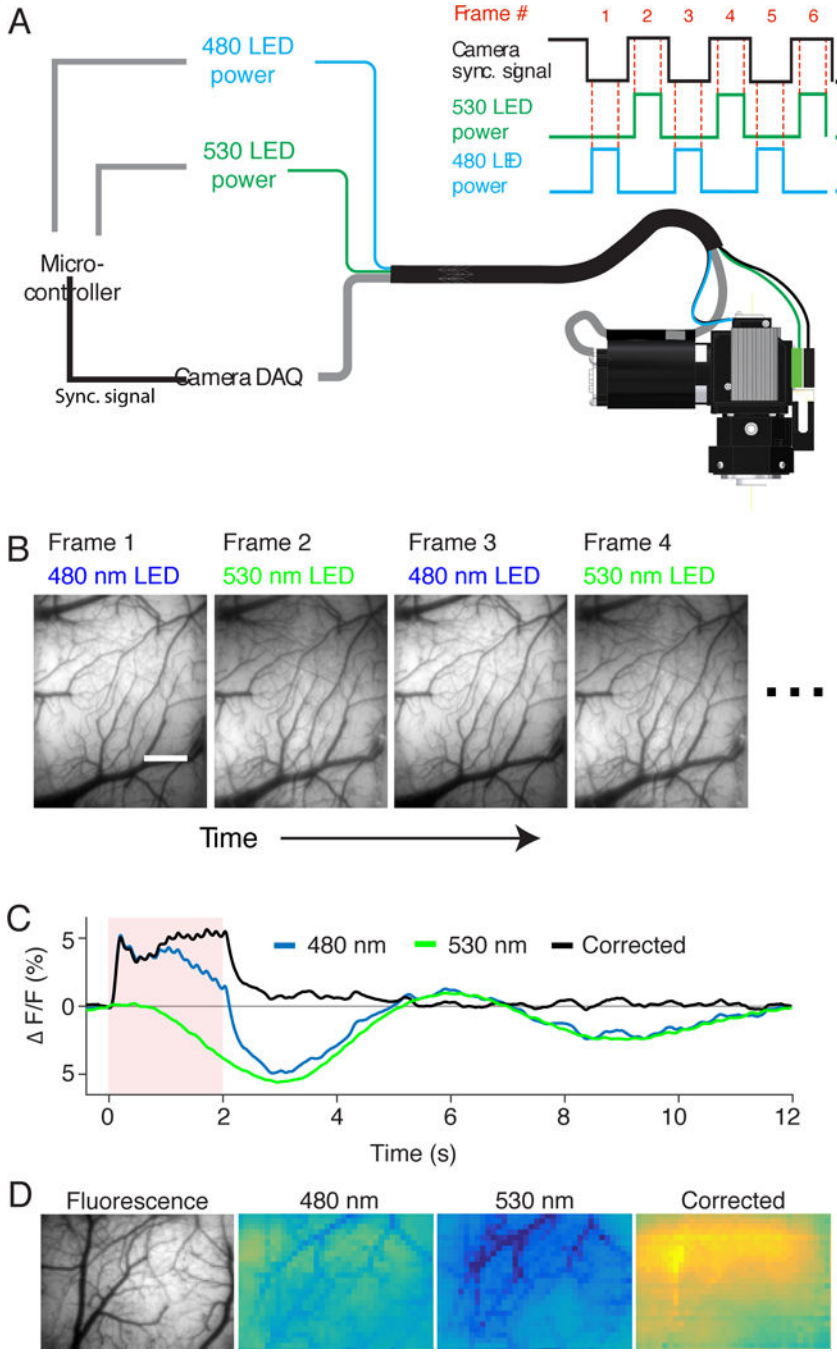

Figure 6.

Hemodynamic correction of fluorescence imaging using a stroboscopic illumination pattern (A) Schematic of the approach used to synchronize stroboscopic blue - green illumination with camera frame exposure. The camera DAQ provides a synchronization signal to a microcontroller which switches between 480 and 530 nm illumination. Upper right insert: Timing of 480 and 530 nm illumination relative to the camera frame exposure. The dashed red vertical lines indicate the timing of each illumination period relative to the frame acquisition. (B) Sequence of four frames acquired with cScope using the stroboscopic

illumination procedure Illustrated in A. (C) Hemodynamic correction of GCaMP6f fluorescence changes during visual stimulation. Blue line indicates the normalized intensity changes (ΔF/F) for blue (480 nm) illumination during a 2-second long visual stimulation period (alternating checkerboard pattern) and a 10-second long inter-stimulus interval (isoluminant gray screen). Green line indicates the normalized intensity changes for green (530 nm) illumination. Black line indicates the corrected ΔF/F changes in GCaMP fluorescence. Pink shaded region indicates the stimulus presentation period. Note that the uncorrected fluorescence signal begins to decline before the end of the visual stimulus, dropping below baseline before recovering. This time course mirrors the dynamics observed with 530 nm illumination. The corrected fluorescence signal remains relatively constant throughout the stimulus period and then decays to baseline suggesting that hemodynamic contamination has been significantly reduced. (D) Spatial response 2 s after the onset visual stimulation before and after correction. *Fluorescence* : Intensity from a single frame acquired with cScope under 480 nm illumination. *480 nm*: ΔF/F for the uncorrected signal recorded at 480 nm. Note the prominent reduction of ΔF/F at the location of the vasculature. *530 nm*: ΔF/F for the uncorrected signal recorded at 530 nm. *Corrected*: ΔF/F for the corrected fluorescence. Note that the vasculature artifacts have been dramatically reduced, providing further evidence that the divisive normalization correction produced implemented by cScope is effective at reducing contamination of the GCaMP signal by the hemodynamic response. See also Figures S6 and S7.

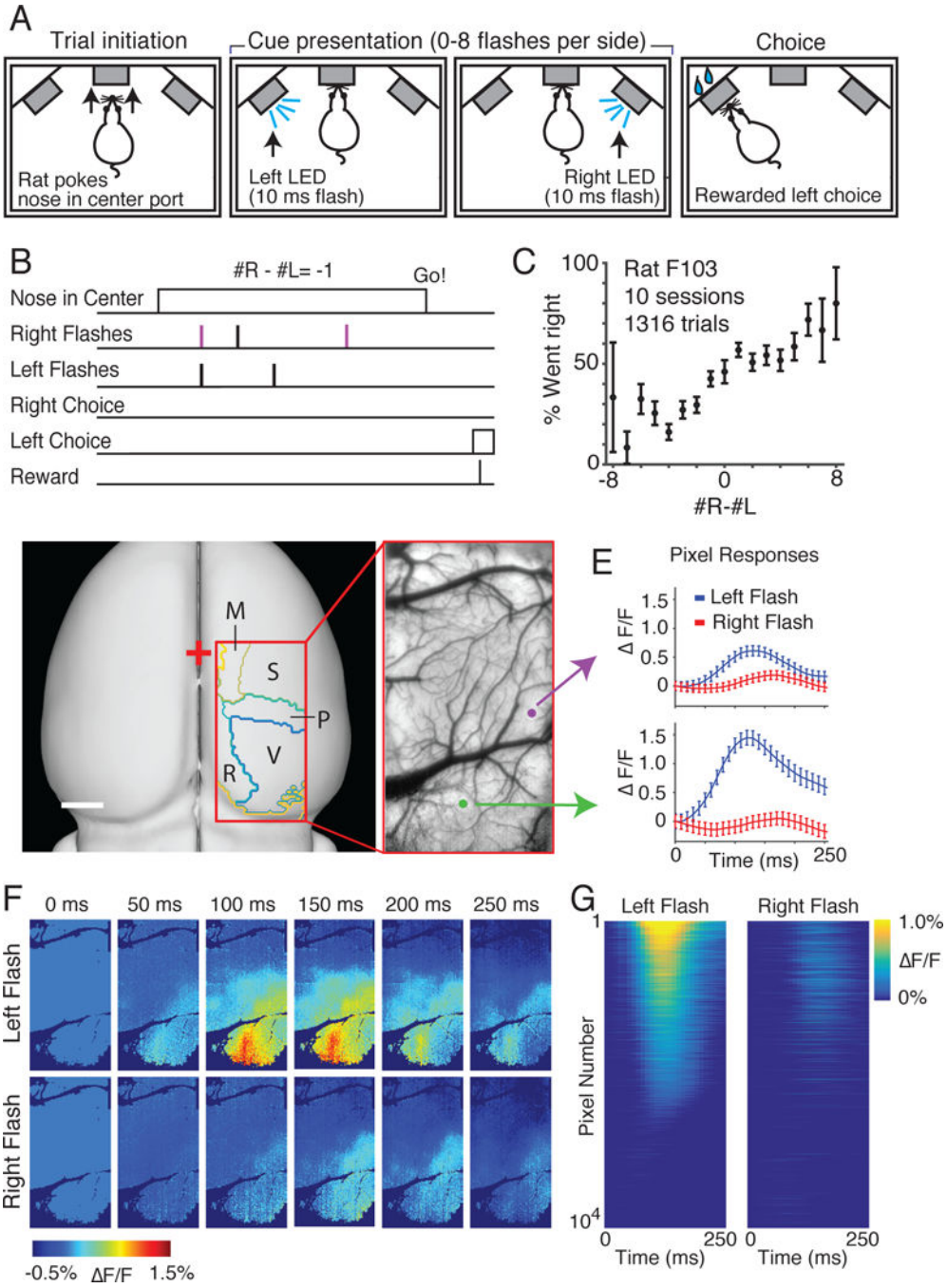

Figure 7.

Mesoscale neocortical calcium dynamics during an evidence accumulation task. (A) Schematic of the evidence accumulation task. Rats initiate a behavioral trial (Trial Initiation, left panel) by inserting their nose into the center port of an operant training chamber. Next, rats view a sequence of up to 8 brief (10ms) flashes from a left and a right LED (Cue presentation, middle panels). After the cue presentation, rats orient to the side port corresponding to the LED with the greater number of flashes to obtain water reward (Choice, right panel). (B) Timing of events during the evidence accumulation task. (C)

Behavioral performance of rat F103 on the task across 10 imaging sessions. (D) Left: Schematic of a rat brain from a dorsal perspective indicating the approximate boundaries of brain regions based on stereotaxic position. Motor (M), Somatosensory (S), Parietal (P), Retrosplenial (R) Visual (V). The black rectangle indicates the location of the camera field of view during the imaging sessions. Right: cScope fluorescence image of the region indicated by the red rectangle in the left panel. Colored dots indicate the location of two ROIs (single pixels) that correspond to the flash response dynamics in E. (E) Average response of two ROIs aligned to the time of left (blue line) and right (red line) flashes. Upper panel corresponds to the dynamics recorded at the location of the purple dot shown in the right panel of D. Lower panel corresponds to the dynamics recorded at the location of the green dot. (F) Timescale of GCaMP fluorescence changes in the right cortical hemisphere following flashes averaged across all single flash events during the cue period of the task during a single behavioral session. Upper panels show dynamics following left flashes only aligned to the time of the flash. Lower panels show dynamics following right flashes only (simultaneous flashes were excluded from the analysis). Flashes were separated in time by a minimum of 250 ms, therefore no secondary flashes occurred in the interval shown. (G) Average response of all pixels aligned to the time of left and right flashes. Each row corresponds to a different pixel and are sorted by magnitude to the response to the left flash. Columns correspond to time points following flashes. Color indicates the average response (ΔF/F) of each pixel at the indicated time.

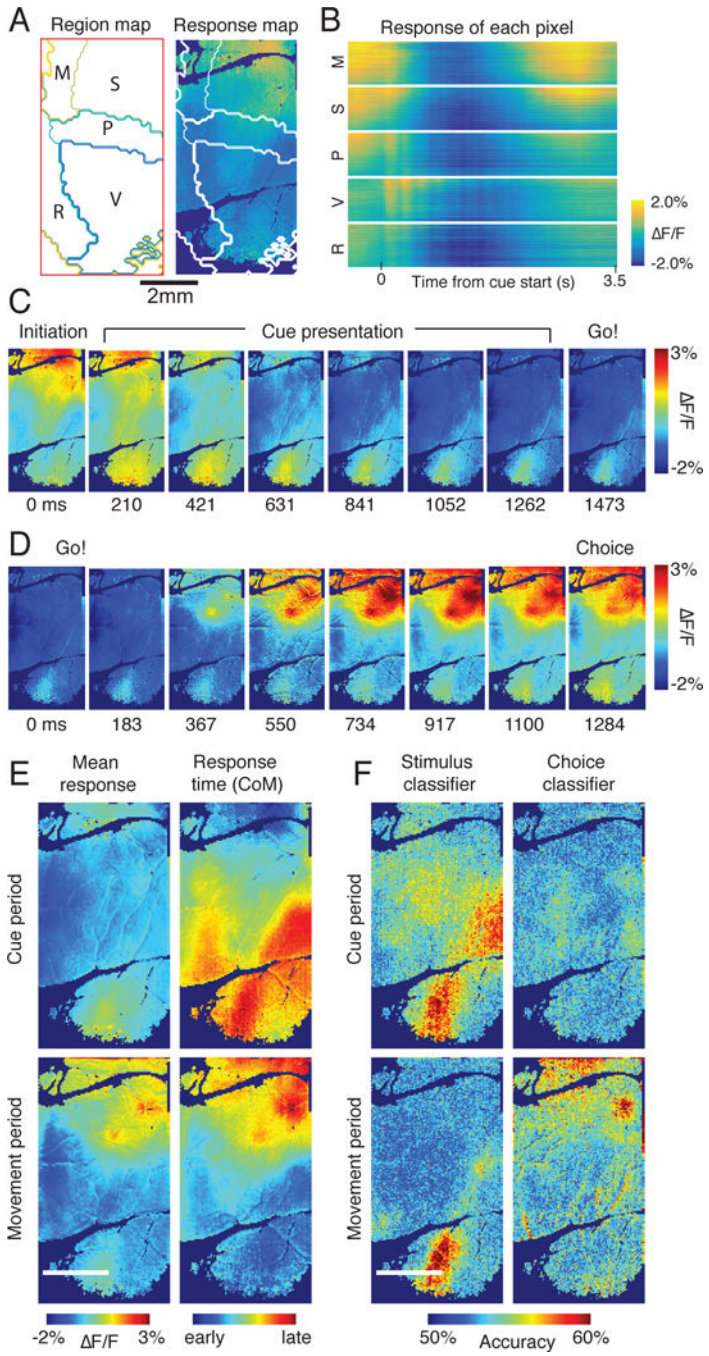

Figure 8.

Spatio-temporal changes in cortical calcium levels correlate with behavioral choice and visual stimulus during evidence accumulation (A) Left: Locations of cortical regions relative to the imaging field of view based on stererotaxic coordinates. Motor (M), Somatosensory (S), Parietal (P), Retrosplenial (R) Visual (V). Right: Regional boundaries (white lines) shown in left superimposed on a map of activity obtained using cScope. (B) Response of each pixel shown in A during the evidence accumulation task. Each row represents the response of an individual pixel in A sorted by brain region. Color indicates the response

(ΔF/F) of that pixel at each timepoint aligned to the start of the cue presentation period and averaged across all trials. (C) Mesoscale pattern of GCaMP fluorescence changes (ΔF/F) during the cue presentation period of the task averaged across all completed trials. (D) Patten of GCaMP fluorescence changes during the movement period of the task averaged across all completed trials. In both panels C and D, dynamics from trials of different durations were time warped to match the duration of the mean. (E) Left panel shows the average GCaMP fluorescence change during the cue presentation (upper left) and movement period (lower left) of the accumulation task. Right panels show the relative timing of the fluorescence changes across the cortex during the cue period (upper right) and movement period (lower right) estimated by computing the "center of mass" (CoM) of each pixel's ΔF/F. (F) GCaMP dynamics correlate with the visual stimulus and the choice of the animal on a trial by trial basis. Pixel color indicates the accuracy of a classifier that uses the GCaMP fluorescence changes on each trial to predict stimulus type, defined as either #R>#L or #R<#L (left panels) or the choice of the animal (right panels). See also Figure S8.

Table 1.

Size and stereotaxic position of cranial window implants

Window size (mm)	Left vertices (mm)	Right vertices (mm)
8 by 8	+4 left; +1AP	+4 right; +1AP
	+4 left; −7 AP	+4 right; −7 AP
8 by 4	+0.75 right; +1AP	+4.75 right; +1AP
	+0.75 right; −7 AP	+4.75 right; −7 AP

Table 2.

Variability in GCaMP fluorescence across animals

Line	Sex	Age (days)	Mean brightness (AU)	Variance (AU)	Generation
7	F	212	2.1716	0.7529	8
7	F	212	2.9448	0.9991	8
7	M	79	1.0000	0.3903	9
7	M	79	2.0172	0.7607	9
9	M	124	2.1565	0.8504	9
9	F	120	1.2928	0.8167	7
9	F	197	1.1125	0.555	7
9	F	197	1.1320	0.5925	7